Alexandria Engineering Journal 112 (2025) 74–83

Contents lists available at ScienceDirect

Alexandria Engineering Journal

journal homepage: www.elsevier.com/locate/aej

Original article

Melting ternary hybrid nanofluid stagnation point flow with velocity slip past a stretching/shrinking sheet: Numerical simulation and validation via P2SATRA

Nur Syahirah Wahid [a,*], Nur Ezlin Zamri [a], Siti Zulaikha Mohd Jamaludin [b], Nur Hazirah Adilla Norzawary [c], Mohd Shareduwan Mohd Kasihmuddin [b], Mohd. Asyraf Mansor [d], Norihan Md Arifin [a,c], Ioan Pop [e,f]

[a] Department of Mathematics and Statistics, Faculty of Science, Universiti Putra Malaysia, Serdang, Selangor 43400 UPM, Malaysia
[b] School of Mathematical Sciences, Universiti Sains Malaysia, Penang 11800 USM, Malaysia
[c] Institute for Mathematical Research, Universiti Putra Malaysia, Serdang, Selangor 43400 UPM, Malaysia
[d] School of Distance Education, Universiti Sains Malaysia, Penang 11800 USM, Malaysia
[e] Department of Mathematics, Babeş-Bolyai University, Cluj-Napoca R-400084, Romania
[f] Academy of Romanian Scientists, 3 Ilfov Street, Bucharest 050044, Romania

ARTICLE INFO

Keywords:
Ternary hybrid nanofluid
Melting
Second-order velocity slip
Stretching/shrinking
Stability analysis
Permutation 2 satisfiability reverse analysis

ABSTRACT

Ternary hybrid nanofluids are crucial to be modeled and researched before their commercial application as a heat transfer fluid. This study investigates the stagnation point flow of a ternary hybrid nanofluid past a stretching/shrinking sheet, focusing on the influence of the melting parameter and second-order velocity slip. The governing partial differential equations (PDEs) are initially formulated and subsequently reduced to ordinary differential equations (ODEs). These ODEs are further transformed into first-order form and numerically solved using the bvp4c solver in MATLAB. Stability analysis is conducted due to the existence of two potential solutions, of which only one proves stable upon analysis. The numerical results indicate significant enhancements in heat transfer performance under conditions of elevated melting and enhanced velocity slip. Reducing the melting parameter and second-order velocity slip may expand the solution range, leading to a delay in boundary layer separation. The stable numerical solution for the heat transfer rate is then validated with the use of a logic mining model namely Permutation 2 Satisfiability Reverse Analysis (P2SATRA). The most accurate induced logic, chosen to illustrate the overall relationship between the selected parameters is achieved in the third fold of a 10-fold cross-validation, yielding an accuracy of 0.81818.

1. Introduction

Nanotechnology has become crucial in fields like electricity generation, chemical processes, cancer treatment, petrochemicals, solar energy, and transportation, and its application in nano-coated high-speed steel tools has revolutionized machining processes by improving tool durability, reducing wear, and enhancing cutting efficiency [1–3]. Recent advancements in nanoparticle production mark a major step forward in enhancing heat transfer methods. By utilizing smaller particles and reducing volume fractions, these innovations tackle issues like pressure drop effectively [4]. In this regard, researchers have recognized ternary hybrid nanofluids as vital for improving heat transfer systems across various industries, including automotive, aerospace, and electronics, harnessing the advantages of nanotechnology to boost thermal efficiency [5]. These advanced fluids incorporate three different types of nanoparticles and are specifically designed to enhance thermal conductivity, stability, and other characteristics compared to traditional heat transfer fluids and binary nanofluids, which only utilize a single type of nanoparticle. As industries continue to search for effective thermal management solutions, the development and use of ternary hybrid nanofluids are attracting increasing interest due to their potential to optimize performance and lower energy consumption in thermal applications.

Several studies have highlighted the superior heat transfer properties of ternary hybrid nanofluids. Manjunatha et al. [6] analyzed the ternary

* Corresponding author.
E-mail address: syahirahwahid@upm.edu.my (N.S. Wahid).

https://doi.org/10.1016/j.aej.2024.10.082
Received 30 September 2024; Received in revised form 15 October 2024; Accepted 21 October 2024
Available online 2 November 2024

Nomenclature

a, c	constants
A_1,B_1	first and second-order velocity slip factors
A, B	first and second order velocity slip parameter
C_f	local skin friction coefficient
C_s	the heat of the solid
L	latent heat of the solid melting
Me	Melting parameter
Nu_x	Local Nusselt number
N	number of neurons
Pr	Prandtl number
Q	logical rule
S_i	final neuron state
T_m	constant melting temperature
T_∞	far-field temperature
$u_w(x)$	sheet velocity
u, v	velocities in (x,y)-directions
$u_e(x)$	far-field velocity
x, y	Cartesian coordinates
η	dimensionless similarity variable
γ	eigenvalues
λ	stretching/shrinking parameter
ϕ	nanoparticle volume fraction
Ω, ω	symbol of parameter used in P2SATRA
τ	dimensionless time variable

hybrid nanofluid past a linear stretching sheet using the Runge-Kutta-Fehlberg-45 (RKF-45) method. Alshahrani et al. [7] studied thermal radiation with slip boundary conditions on ternary hybrid nanofluid over a spinning disc, concluding that ternary hybrid nanofluids exhibit better heat transfer properties than traditional fluids, nanofluids, and hybrid nanofluids. Riaz et al. [8] investigated ternary hybrid nanofluid flow over a linearly stretching surface, while Mahabaleshwar et al. [9] analyzed ternary hybrid nanofluid flow past a Riga plate with Newtonian heating effect using the shooting method and the bvp4c algorithm, finding that a heat source elevates the rate of heat transfer. Jan et al. [10] examined the impact of variable thermal conductivity of ternary hybrid nanofluids over a stretching sheet with magnetic field and convective boundary conditions, and they reported that both skin friction and the Nusselt number declined as the slip factor increased. Jamrus et al. [11] explored the flow of thermally stratified ternary hybrid nanofluid with magnetohydrodynamic and mixed convective over a stretching/shrinking sheet, considering velocity slip, and concluded that a higher volume fraction of the ternary hybrid nanofluid enhanced its heat transfer capabilities. Other latest literature on ternary hybrid nanofluids also include the work by Mahmood et al. [12] and Ishak et al. [13].

Melting heat transfer is a critical process in numerous scientific and engineering applications, involving the transfer of heat to a solid material, causing it to convert from solid to liquid. Mastering this process is essential in fields such as metallurgy, manufacturing, thermal energy storage, and environmental engineering. Roberts [14] first established the concept of heat transfer, inspiring further research into the properties and mechanisms of melting heat transfer. Epstein and Cho [15] examined melting heat transfer in flat plate laminar flow, leading to additional studies on the effects of various geometries and fluids on this process. Bachok et al. [16] studied melting heat transfer in a heated, laminar stagnation point flow over a stretching/shrinking, while Ahmad and Pop [17] analyzed the impact of the melting parameter on mixed convective flow in a porous geometry. Muhammad et al. [18] simulated the magnetohydrodynamic nanofluid flow under conditions of velocity slip, melting, and radiative heat transfer which contributed to the growing body of research on melting heat transfer. Some studies that have incorporated the effect of melting in their research are as follows: [19–23].

Given the significance of slip boundary conditions in fluid flow, Norzawary et al. [24,25] investigated slip flow via linearly and exponentially stretching/shrinking sheets in carbon nanotubes (CNTs), and they reported that the increment of slip parameter broadens the solution range. Second-order slip, a higher-order approximation in fluid flow studies, particularly in microfluidics and gas dynamics, provides a more accurate description of the velocity profile near the boundary. Roşca and Pop [26] investigated the flow and heat transfer with second-order slip, highlighting the necessity of the second-order slip flow model for accurate predictions. Hakeem et al. [27] also studied the nanofluid slip flow, concluding that both the magnetic field and second-order slip significantly affected the flow characteristics. Uddin et al. [28] analyzed the nanofluid flow with melting and second-order slip effect, finding that the friction factor decreases with slip and melting parameters for both stretching/shrinking sheets, while the Nusselt number reduces with first-order slip but increases with the melting parameter. Bakar et al. [29] researched the hybrid nanofluid flow with a Darcy–Forchheimer porous medium over a permeable shrinking surface with second-order velocity slip, summarizing that hybrid nanofluids present higher heat and mass transfer rates than classic mono-nanofluids. Recently, Swapna et al. [30] investigated the Casson nanofluid flow with chemical reaction and viscous dissipation with the slip effect and reported that the slip effect has reduces the skin friction.

Existing literature on using Artificial Intelligence (AI) methods as the validation medium for fluid dynamics has expanded over the years. This has shown significant reliability and accuracy of AI methods to validate computational fluid dynamics simulations. Pioneer work by Oberkampf and Trucano [31] stated that the fundamental strategy of AI validation for fluid dynamics is to assess how accurate the extracted computational results are with the experimental data trained by AI. Conjointly, this approach breaks down and clarifies the physical and interrelated processes in the complex engineering system. Existing work by Alhadri et al. [32] employed a fundamental Artificial Neural Network (ANN) to predict the interest physical quantities which as the skin friction coefficient and local Nusselt number. The ANN model is composed of six neurons that represent the parameters that control such physical quantities. The measured mean square error (MSE) between the obtained results to the predicted results using ANN showed promising validation experimentation with an MSE average of MSE (average) = 0.02 across different number of epochs. However, the evaluated value of correlation coefficient or for the subset of training data is higher than the testing data. This indicates that the employed ANN produced overfitting solutions of the *Nux* whereby the results are extremely sensitive to any changes of parameter values for another generation of *Nux*.

Another attempt was made by Sharma et al. [21] where the existing work utilized Marquardt backpropagation neural network (MBNN) to validate the numerical results from the model of Darcy-Forchheimer hybrid nanofluid flow with of chemical reaction. The suggested MBNN executed fined tuning synaptic weights via backpropagation and feeding the loss backwards through the neural network layers. Based on the MSE results of six parameters, the MBNN can converge at an epoch equal to 12. Similar to the previous work, the output produced by MBNN can only make sense to the presence entries of the model and cannot be generalized to future numerical results of the model. Recently, Reddisekhar Reddy et al. [33] proposed the use of backpropagation via a neural network to predict the numerical results of a hybrid nanofluid with Thompson and Troian slip boundary condition over a porous cylinder. The existing works attained relatively low MSE values with a smaller number of iterations needed to converge towards an acceptable

range of the numerical results. While all of the mentioned existing works offered plausible validation approaches of fluid flow problems, all existing works employed outdated AI validation methods that are unable to produce non-overfitting solutions. In this context, non-overfitting and interpretable outputs via AI are crucial to offer generalizability property for other fluid flow problems that usually affected by similar parameters. It is imperative to implement an AI validation approach that has the ability to classify or predict future/ another generation of the numerical results for any fluid flow related problems without having to retrain the AI model.

Motivated by preceding work, this study aims to formulate and solve the model of ternary hybrid nanofluid stagnation point flow past a stretching/shrinking sheet with second-order velocity slip and melting effect. Building on Waini et al. [34], who studied a similar model configuration with a hybrid nanofluid, this research extends the model to a ternary hybrid nanofluid. This research presents a novel approach by developing a boundary layer flow model for melting ternary hybrid nanofluid under stagnation point condition past a stretching/shrinking sheet, incorporating second-order velocity slip. The governing PDEs are formulated and converted into ODEs, which are then solved numerically using a finite difference scheme. Although two solutions are obtained, stability analysis verifies that only one is stable (first solution). Further validation of this stable solution is achieved through logic mining using P2SATRA, to provide additional insights and representations to assess the heat transfer rate of the fluid flow system.

2. Model formulation

Consider the two-dimensional steady stagnation point boundary layer flow of an incompressible ternary hybrid nanofluid along a permeable stretching/shrinking sheet, as it is shown in Fig. 1. The velocity of the stretching/shrinking sheet is assumed to be $u_w(x) = cx$ and the far-field velocity is $u_e(x) = ax$, where a and c are constants. The first and the second order velocity slip factors are A_1 and B_1 respectively, the constant melting temperature is T_m, and the temperature of the far-field is T_∞.

With the given assumptions, the model can be formulated as follows consisting of the continuity, momentum, and energy equations (see Manjunatha et al. [6]; Waini et al. [34]; Bachok et al. [16]):

$$\frac{\partial u}{\partial x}+\frac{\partial v}{\partial y}=0, \tag{1}$$

$$\begin{aligned} &u\frac{\partial u}{\partial x}+v\frac{\partial u}{\partial y}=\frac{\mu_{thnf}}{\rho_{thnf}}\frac{\partial^2 u}{\partial y^2}+u_e\frac{du_e}{dx},\\ &u=U_w(x)=u_w(x)+A_1\frac{\partial u}{\partial y}+B_1\frac{\partial^2 u}{\partial y^2}=cx+A_1\frac{\partial u}{\partial y}+B_1\frac{\partial^2 u}{\partial y^2}\ \text{at}\ y=0,\\ &u\to u_e(x)\ \text{as}\ y\to\infty, \end{aligned} \tag{2}$$

$$\begin{aligned} &u\frac{\partial T}{\partial x}+v\frac{\partial T}{\partial y}=\frac{k_{thnf}}{(\rho C_p)_{thnf}}\frac{\partial^2 T}{\partial y^2},\\ &T=T_m,\ \left(\frac{k_{thnf}}{\rho_{thnf}}\right)\frac{\partial T}{\partial y}=(L+C_s(T_m-T_0))v(x,0)\ \text{at}\ y=0,\\ &T\to T_\infty\ \text{as}\ y\to\infty, \end{aligned} \tag{3}$$

where (u, v) are the velocity components along (x, y) – axes, C_s is the heat of the solid, and L is the latent heat of the solid melting. Further, the thermophysical properties model of ternary hybrid nanofluid is defined in Table 1.

Here, $\phi_i, (i = 1, 2, 3)$ are the nanoparticle volume fractions such that the subscripts of 1, 2, and 3 refer to alumina nanoparticle, copper nanoparticle, and silver nanoparticle, respectively, while $\phi_i = 0$ correspond to a regular fluid. The subscript of $thnf, hnf, nf$ and f refers to the ternary hybrid nanofluid, hybrid nanofluid, nanofluid, and base fluid, respectively. The thermophysical properties of the base fluid which is water (H_2O), alumina (Al_2O_3), copper (Cu), and silver (Ag) are given in Table 2.

For the sake of simplicity, the subsequent similarity variables are introduced:

$$u=axf'(\eta), v=-\sqrt{av_f}f(\eta), T=\theta(\eta)(T_\infty-T_m)+T_m, \eta=y\sqrt{\frac{a}{\nu_f}}, \tag{4}$$

Substituting Eq. (4) into Eqs. (2) and (3), they are reduced to the boundary value problem as follows

$$\begin{aligned} &\left(\frac{\mu_{thnf}/\mu_f}{\rho_{thnf}/\rho_f}\right)f'''-f'^2+ff''+1=0,\\ &f'(0)=\lambda+Af''(0)+Bf'''(0),\ f'(\infty)\to 1, \end{aligned} \tag{5}$$

$$\begin{aligned} &\frac{1}{\Pr}\left(\frac{k_{thnf}/k_f}{(\rho C_p)_{thnf}/(\rho C_p)_f}\right)\theta''+f\theta'=0,\\ &\theta(0)=0,\ Me\left(\frac{k_{thnf}/k_f}{\rho_{thnf}/\rho_f}\right)\theta'(0)+\Pr f(0)=0,\ \theta(\infty)\to 1, \end{aligned} \tag{6}$$

where Pr is the Prandtl number, Me is the melting parameter, $A > 0$ is

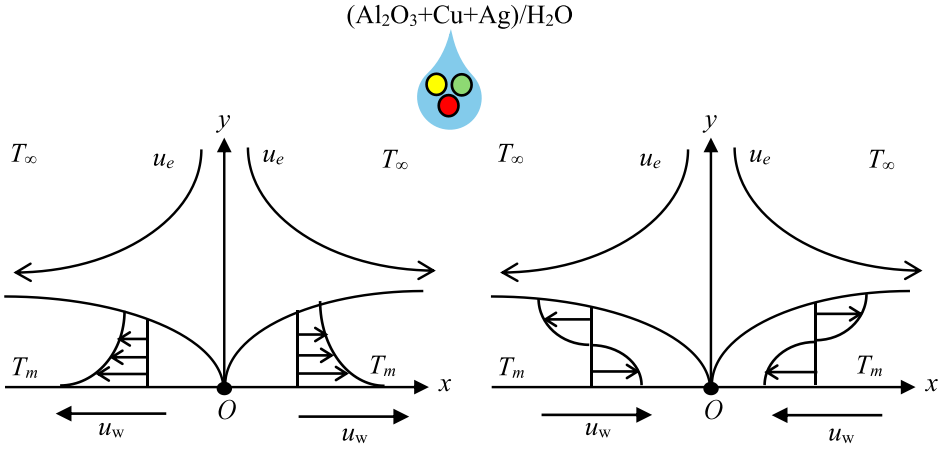

Fig. 1. Physical model of the ternary hybrid nanofluid flow past a stretching (left) and shrinking (right) sheet.

Table 1
Thermophysical properties model of ternary hybrid nanofluid ([6,35]).

Properties	Model
Dynamic viscosity	$\mu_{thnf} = \frac{\mu_f}{(1-\phi_1)^{2.5}(1-\phi_2)^{2.5}(1-\phi_3)^{2.5}}$
Density	$\rho_{thnf} = (1-\phi_3)\{(1-\phi_2)[(1-\phi_1)\rho_f + \phi_1\rho_1] + \phi_2\rho_2\} + \phi_3\rho_3$
Heat capacitance	$(\rho C_p)_{thnf} = (1-\phi_3)\{(1-\phi_2)[(1-\phi_1)(\rho C_p)_f + \phi_1(\rho C_p)_1] + \phi_2(\rho C_p)_2\} + \phi_3(\rho C_p)_3$
Thermal conductivity	$k_{thnf} = \frac{k_3 + 2k_{hnf} - 2\phi_3(k_{hnf} - k_3)}{k_3 + 2k_{hnf} + \phi_3(k_{hnf} - k_3)} \times k_{hnf}$ where $k_{hnf} = \frac{k_2 + 2k_{nf} - 2\phi_2(k_{nf} - k_2)}{k_2 + 2k_{nf} + \phi_2(k_{nf} - k_2)} \times k_{nf}$ and $k_{nf} = \frac{k_1 + 2k_f - 2\phi_1(k_f - k_1)}{k_1 + 2k_f + \phi_1(k_f - k_1)} \times k_f$

Table 2
Considered values for the thermophysical properties (see Ishak et al. [36]).

Properties	H_2O	Al_2O_3	Cu	Ag
$\rho\left(\mathrm{kg/m^3}\right)$	997.1	3970	8933	10500
C_p(J/kgK)	4179	765	385	235
k(W/mK)	0.613	40	400	429
Pr	6.2	NA	NA	NA

the first-order velocity slip parameter, $B < 0$ is the second-order velocity slip parameters and λ is the stretching/shrinking parameter, with $\lambda > 0$ for the stretching, $\lambda < 0$ for the shrinking and $\lambda = 0$ for the static sheet, which are defined as

$$\mathrm{Pr} = \frac{(\mu C_p)_f}{k_f},\ Me = \frac{(C_p)_f(T_\infty - T_m)}{L + C_s(T_m - T_0)},\ A = A_1\sqrt{\frac{a}{\nu_f}},\ B = B_1\frac{a}{\nu_f},\ \lambda = \frac{c}{a}. \tag{7}$$

The model is analyzed through the physical quantities of interest which are the skin friction coefficient C_f and the local Nusselt number Nu_x:

$$C_f = \frac{\mu_{thnf}}{\rho_f u_e^2(x)}\left(\frac{\partial u}{\partial y}\right)_{y=0},\ Nu_x = \frac{xk_{thnf}}{k_f(T_\infty - T_m)}\left(-\frac{\partial T}{\partial y}\right)_{y=0}. \tag{8}$$

Using Eq. (4) in Eq. (8), we get

$$\mathrm{Re}_x^{1/2}C_f = \frac{\mu_{thnf}}{\mu_f}f''(0), \mathrm{Re}_x^{-1/2}Nu_x = -\frac{k_{thnf}}{k_f}\theta'(0), \tag{9}$$

where Re_x is the local Reynolds number.

2.1. Stability analysis

It is required to conduct the stability analysis when more than one solution exists [37]. To perform the stability analysis, the problem model is considered to be unsteady. Based on Eq. (4), the dimensionless variables are

$$u = ax\frac{\partial f(\eta,\tau)}{\partial \eta},\ v = -\sqrt{a\nu_f}f(\eta,\tau),\ T = \theta(\eta,\tau)(T_\infty - T_m) + T_m,\ \eta = y\sqrt{\frac{a}{\nu_f}},\ \tau = at. \tag{10}$$

The use of τ relates to an initial value problem, determining the physically realizable solution. Thus, Eqs. (5) and (6) can be expressed as:

$$\left(\frac{\mu_{thnf}/\mu_f}{\rho_{thnf}/\rho_f}\right)\frac{\partial^3 f}{\partial \eta^3} + f\frac{\partial^2 f}{\partial \eta^2} - \left(\frac{\partial f}{\partial \eta}\right)^2 - \frac{\partial^2 f}{\partial \eta \partial \tau} + 1 = 0,$$
$$\frac{\partial f(0,\tau)}{\partial \eta} = \lambda + A\frac{\partial^2 f(0,\tau)}{\partial \eta^2} + B\frac{\partial^3 f(0,\tau)}{\partial \eta^3},\ \frac{\partial f(\infty,\tau)}{\partial \eta} \to 1, \tag{11}$$

$$\frac{1}{\mathrm{Pr}}\left(\frac{k_{thnf}/k_f}{(\rho C_p)_{thnf}/(\rho C_p)_f}\right)\frac{\partial^2 \theta}{\partial \eta^2} + f\frac{\partial \theta}{\partial \eta} - \frac{\partial \theta}{\partial \tau} = 0,$$
$$\theta(0,\tau) = 0,\ Me\left(\frac{k_{thnf}/k_f}{\rho_{thnf}/\rho_f}\right)\frac{\partial \theta(0,\tau)}{\partial \eta} + \mathrm{Pr}f(0,\tau) = 0,\ \theta(\infty,\tau) \to 1. \tag{12}$$

Next, the perturbation relations are introduced, as follows [38]:

$$f(\eta,\tau) = f_0(\eta) + e^{-\gamma\tau}F(\eta,\tau),\ \theta(\eta,\tau) = \theta_0(\eta) + e^{-\gamma\tau}G(\eta,\tau), \tag{13}$$

where γ is an unknown eigenvalue parameter, and $F(\eta,\tau)$ and $G(\eta,\tau)$ are small relative to $f_0(\eta)$ and $\theta_0(\eta)$, respectively. Applying Eq. (13) into Eqs. (11) and (12), and by setting $\tau = 0$ (steady flow), the growth or decay of the perturbation can be analyzed. Putting $\tau = 0$ leads us to $F(\eta,0) = F_0(\eta)$ and $G(\eta,0) = G_0(\eta)$. Finally, the linear eigenvalue problem that needs to be solved is as follows:

$$\left(\frac{\mu_{thnf}/\mu_f}{\rho_{thnf}/\rho_f}\right)F_0''' + f_0F_0'' + F_0f_0'' - 2f_0'F_0' + \gamma F_0' = 0,$$
$$F_0'(0) = AF_0''(0) + BF_0'''(0),\ F_0'(\infty) \to 0, \tag{14}$$

$$\frac{1}{\mathrm{Pr}}\left(\frac{k_{thnf}/k_f}{(\rho C_p)_{thnf}/(\rho C_p)_f}\right)G_0'' + f_0G_0' + F_0\theta_0' + \gamma G_0 = 0,$$
$$G_0(0) = 0,\ Me\left(\frac{k_{thnf}/k_f}{\rho_{thnf}/\rho_f}\right)G_0'(0) + \mathrm{Pr}F_0(0) = 0,\ G_0(\infty) \to 0, \tag{15}$$

For the present problem, following the recommendation by Harris et al. [39], the condition of $F_0(\eta)$ as $\eta \to \infty$ is relaxed and is substituted with $F_0''(0) \to 1$. The stability of the steady flow solution is determined by the smallest eigenvalues γ_1 such that if it is positive, then the solution is stable (due to decay of perturbance) but if it is negative, then the solution is not stable (due to growth of perturbance).

3. Validation via Permutation 2 Satisfiability Reverse Analysis (P2SATRA)

A logic mining method called P2SATRA is employed to extract logical rules from datasets (see [40,41] for details). Its primary objective is to determine the most optimal logical rule, such that

$$Q_{2SAT} = \bigwedge_{i=1}^{J} clauses_i, clauses_i = (\Omega_i \vee \omega_i) \tag{16}$$

where $J = 3$, which aligns with the local field computation using Eq. (17) as follows:

$$S_i = \begin{cases} 1, HTAF\left[\sum_{i=1, i\neq j}^{N} W_{ij}^{(2)}S_j + W_i^{(1)}\right] \geq 0 \\ -1, HTAF\left[\sum_{i=1, i\neq j}^{N} W_{ij}^{(2)}S_j + W_i^{(1)}\right] < 0 \end{cases} \tag{17}$$

where S_i is a final neuron state. In the conventional 2SATRA approach introduced by [20], variables are selected at random, which can lead to suboptimal logic generation. Likewise, neurons are arranged in a random order before the Discrete Hopfield Neural Network (DHNN) begins its learning phase.

The attributes $S_i = (S_1, S_2, S_3, \ldots, S_N)$ with N number of neurons is converted into bipolar interpretation $S_i = \{-1, 1\}$. The number of possible neuron permutations after considering the learning logic Q_i^l structure is $N!/[2(N-d)!]$ such that the 2SATRA is required to select d neurons that will be learned by P2SATRA. We can optimally choose the pair of S_i for each clause by considering the relation between Q_i^l and neuron S_i. The S_i selection for each clause is given as follows:

$$Q_{2SAT}^{best} = \max\left[n\left(clauses_{ii}^{(2)}\right)\right], Q_{2SAT}^{train} = 1 \tag{18}$$

where $n\left(clauses_{ii}^{(2)}\right)$ is the number of $\left(clauses_{ii}^{(2)}\right)$ structure that leads to $Q_{2SAT}^{train} = 1$. The final neuron state will be transformed into induced literal according to the following definition:

$$S_i^{induced} = \begin{cases} (\Omega_i \vee \omega_i), & if\ (S_i, S_j) = (1,1) \\ (\Omega_i \vee \neg\, \omega_i), & if\ (S_i, S_j) = (1,-1) \\ (\neg\, \Omega_i \vee \omega_i), & if\ (S_i, S_j) = (-1,1) \\ (\neg\, \Omega_i \vee \neg\, \omega_i), & else\ (S_i, S_j) = (-1,-1) \end{cases} \tag{19}$$

It should be noted that this logic mining P2SATRA approach is utilized to validate the numerical findings. As opposed to other machine learning methods, logic mining via P2SATRA is able to offer interpretability of the output produced by the ANN through the formulation of Satisfiability (SAT). The SAT logic generates clear OR-AND rules that can be easily understood and interpreted which counters the issue of black box models for most ANN models. Because the output of P2SATRA is in the form of SAT logical rules, the insights are immediately actionable. These rules can be directly implemented as pattern guidelines for future boundary layer flow problems when different parameters are involved.

4. Results and discussion

4.1. Numerical

The numerical solver bvp4c in MATLAB is used to address the ODEs of the model [42,43]. This solver employs a finite difference scheme, which is particularly effective for solving boundary value problems with high accuracy. The numerical solutions generated include the skin friction coefficient, local Nusselt number, velocity profile, and temperature profile. These parameters are critical for understanding the flow dynamics and heat transfer characteristics within the system. Before generating these solutions, validation of the numerical computations performed by the bvp4c solver is essential. The validation process involves comparing the numerical results with those reported in the existing literature. Tables 3 and 4 illustrate a comparison of these results with those from earlier studies and the results are seen to be in a well agreement.

The impact of *Me* towards the ternary hybrid nanofluid in terms of $\mathrm{Re}_x^{1/2}C_f$ and $\mathrm{Re}_x^{-1/2}Nu_x$ are shown in Figs. 2 and 3, respectively, versus the value of λ. Two solutions can be generated especially in the range of negative λ. The insertion of a higher melting parameter which in this case is $Me = 3$, is observed to increase the value of $\mathrm{Re}_x^{1/2}C_f$ for the first solution but not for the second solution. The observed trend from the first solution is presumably true because the melting parameter increases skin friction when the sheet is shrinking by promoting more melting, which creates a liquid layer that raises viscosity and resistance to flow near the surface. However, for the value of $\mathrm{Re}_x^{-1/2}Nu_x$, the increment of *Me* leads to the increment of $\mathrm{Re}_x^{-1/2}Nu_x$ as well for both the first and the second solution. Logically, the increase in the melting parameter facilitates the phase change from solid to liquid, which can eventually enhance the heat transfer rate. In the context of boundary layer separation, the increment of *Me* causes the value of the critical point to increase which narrows the range of the solutions. This implies that the higher the considered *Me*, the quicker the separation of the boundary layer from laminar to turbulent. A higher *Me* value is advantageous for achieving superior heat transfer performance, as indicated by the increase $\mathrm{Re}_x^{-1/2}Nu_x$. However, it also induces earlier boundary layer separation and a quicker transition from laminar to turbulent flow, which can negatively impact the stability of the fluid flow. Therefore, the selection of *Me* should balance the need for enhanced heat transfer with the requirement for maintaining flow stability, suggesting that moderate *Me* values may often provide an optimal compromise between these competing effects.

The plots of $\mathrm{Re}_x^{1/2}C_f$ and $\mathrm{Re}_x^{-1/2}Nu_x$ versus λ for different values of B are illustrated in Figs. 4 and 5, respectively. From these figures, as B changes from -1, -2, to -3, the value of $\mathrm{Re}_x^{1/2}C_f$ is observed to reduce in the case of the first solution but oppositely for the second solution. The same pattern is observed to occur in Fig. 5, the behavior of the second solution for $\mathrm{Re}_x^{-1/2}Nu_x$ is not consistent as B changes from -1, -2, to -3. In the context of boundary layer separation, as B changes from -1, -2, to -3, or reducing, the critical point is also reducing and widening the range of the solutions. Hence, this also implies that as B is getting smaller and near to absent, the boundary layer separation is delayed, and the laminar flow phase can be maintained for a longer period. Larger B leads to increased $\mathrm{Re}_x^{1/2}C_f$ and $\mathrm{Re}_x^{-1/2}Nu_x$, but it also accelerates boundary layer separation which illustrates a trade-off where higher B can enhance heat transfer and drag while potentially compromising boundary layer stability.

Figs. 6 and 7 display the velocity and temperature profile for the case of different selection values of *Me* under the configuration of $\lambda = B = -1$, $A = 1$, and $\phi_1 = \phi_2 = \phi_3 = 1\%$. The increment of *Me* has led to the

Table 3
Values of $\mathrm{Re}_x^{1/2}C_f$ when $\phi_1 = \phi_2 = 5\%$ and $\phi_3 = 0$.

λ	*Me*	*A*	*B*	First solution		Second solution	
				Present	Waini et al. [34]	Present	Waini et al. [34]
−1.5	1	1	−1	1.201592062	1.201592	1.132467821	1.132468
−2				1.471525856	1.471526	1.566942168	1.566942
−2.5				1.766345602	1.766346	1.900742700	1.900743
−2	2			1.492622454	1.492622	1.566526965	1.566527
	3			1.506376254	1.506376	1.566125979	1.566126
	5			1.523651020	1.523651	1.565363708	1.565364
	1	1.5		1.216910000	1.216910	1.176685368	1.176685
		2		1.043043302	1.043043	0.910671885	0.910672
		3		0.815485894	0.815486	0.602540155	0.602540
		1	−2	1.035227243	1.035227	1.711669665	1.711670
			−3	0.784415505	0.784416	1.762599767	1.762600
			−4	0.628670532	0.628671	1.787619235	1.787619

Table 4
Values of $\mathrm{Re}_x^{-1/2}Nu_x$ when $\phi_1 = \phi_2 = 5\%$ and $\phi_3 = 0$.

λ	Me	A	B	First solution		Second solution	
				Present	Waini et al. [34]	Present	Waini et al. [34]
−1.5	1	1	−1	−1.250473118	−1.250473	−0.002027924	−0.002028
−2				−1.118551005	−1.118551	−0.033334543	−0.033335
−2.5				−0.924927580	−0.924928	−0.169714023	−0.169714
−2	2			−0.868882153	−0.868882	−0.033025493	−0.033025
	3			−0.715158182	−0.715158	−0.032727794	−0.032728
	5			−0.532929440	−0.532929	−0.032163834	−0.032164
	1	1.5		−1.243700115	−1.243700	−0.002853729	−0.002854
		2		−1.316732510	−1.316733	−0.000272854	−0.000273
		3		−1.401824945	−1.401825	−0.000004469	−0.000004
		1	−2	−1.319834679	−1.319835	−0.069351317	−0.069351
			−3	−1.412692958	−1.412693	−0.088528847	−0.088529
			−4	−1.464885521	−1.464886	−0.099642983	−0.099643

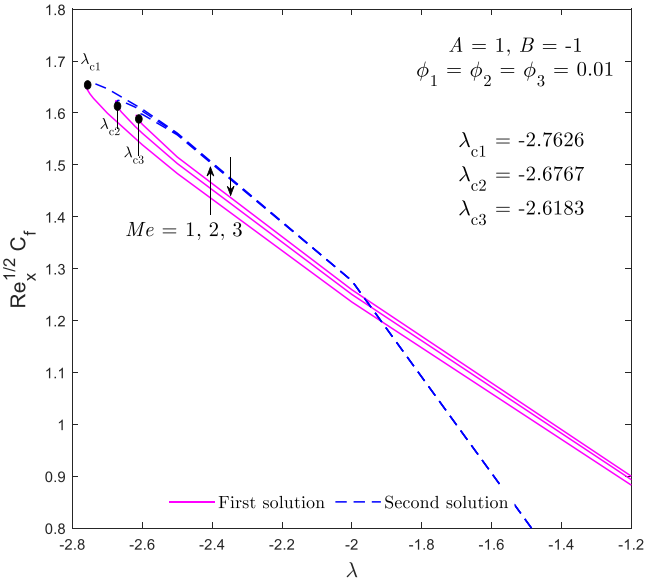

Fig. 2. Plot of $\mathrm{Re}_x^{1/2}C_f$ for different melting parameter.

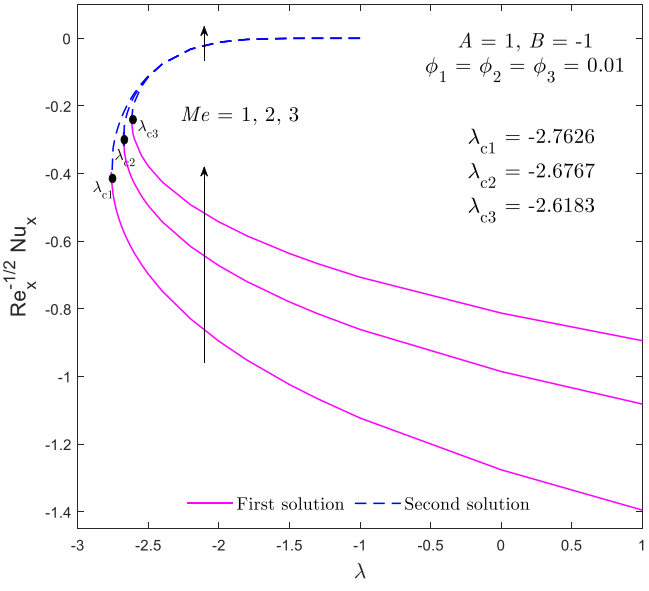

Fig. 3. Plot of $\mathrm{Re}_x^{-1/2}Nu_x$ for different melting parameter.

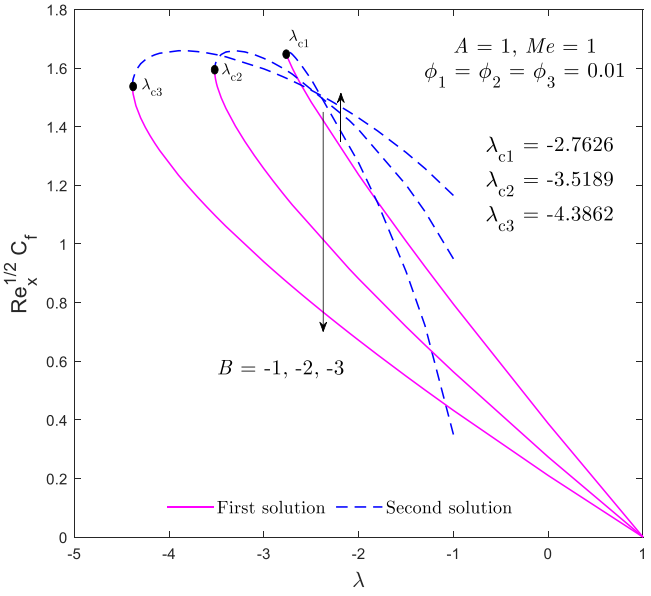

Fig. 4. Plot of $\mathrm{Re}_x^{1/2}C_f$ for different velocity slip (second-order) parameter.

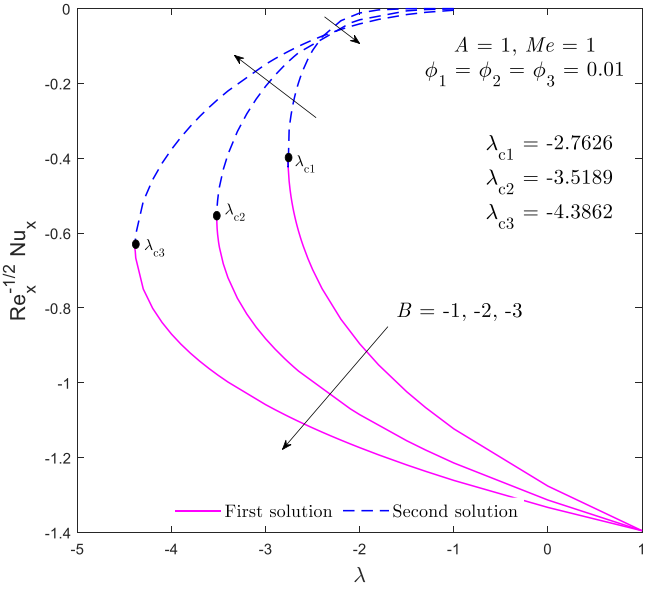

Fig. 5. Plot of $\mathrm{Re}_x^{-1/2}Nu_x$ for different velocity slip (second-order) parameter.

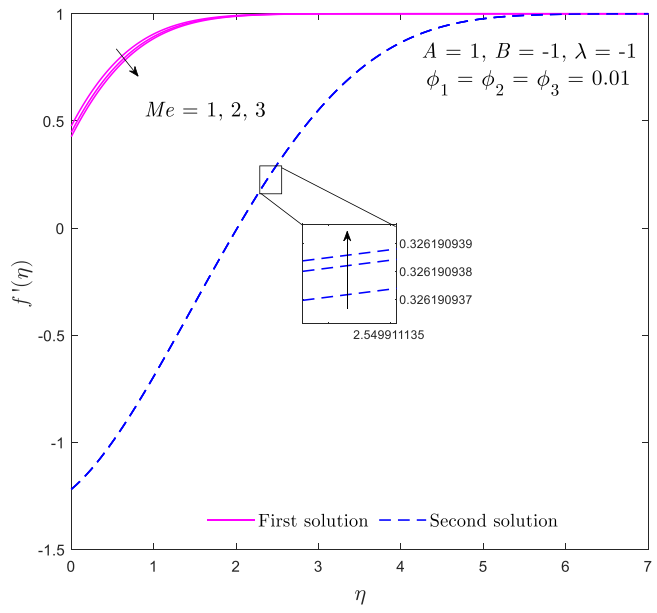

Fig. 6. Plot of $f'(\eta)$ for different melting parameter.

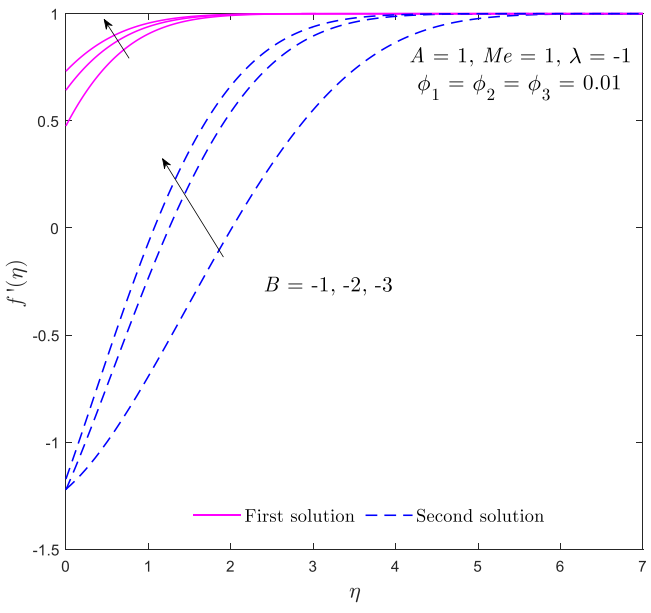

Fig. 8. Plot of $f'(\eta)$ for different velocity slip (second-order) parameter.

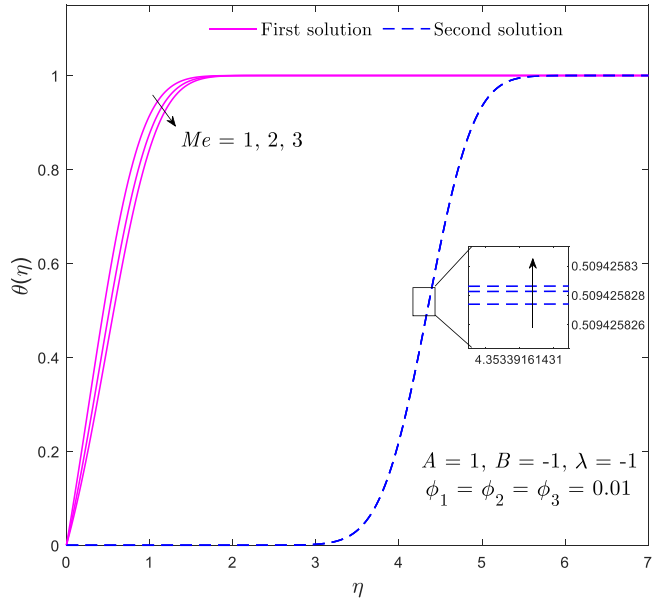

Fig. 7. Plot of $\theta(\eta)$ for different melting parameter.

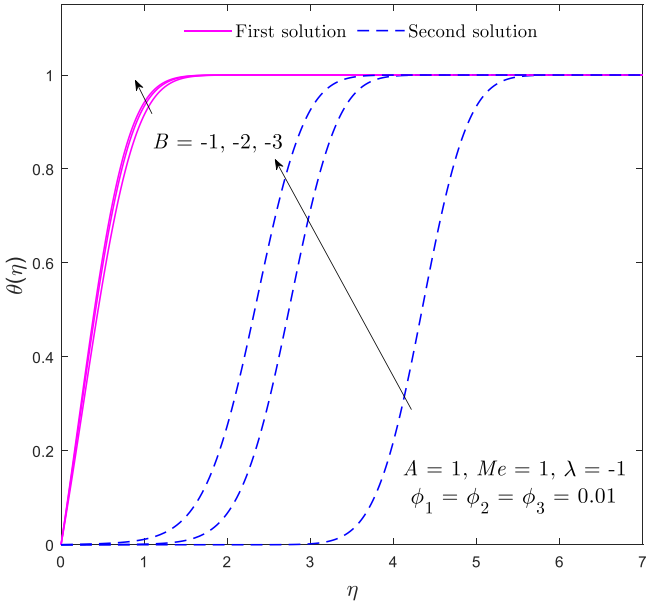

Fig. 9. Plot of $\theta(\eta)$ for different velocity slip (second-order) parameter.

reduction of $f'(\eta)$ and $\theta(\eta)$ as well as thickening the momentum and the thermal boundary layer thickness as shown by the first solution, but the opposite occur for the second solution. The finding given by the first solution is logically true because the increase in the melting parameter facilitates the phase change from solid to liquid, which absorbs heat and results in a reduction of temperature at the shrinking surface. Meanwhile, Figs. 8 and 9 display the velocity and temperature profile for the case of different selection values of B under the configuration of $\lambda = -1$, $A = Me = 1$, and $\phi_1 = \phi_2 = \phi_3 = 1\%$. Both solutions and both velocity profiles under this configuration is increasing with the increasing value of B which also causes the momentum and the thermal boundary layer thickness to decrease.

4.2. Stability

For the stability analysis, the results are illustrated in Fig. 10, which plots the smallest eigenvalues against λ. The first solution yields the positive smallest eigenvalues, indicating stability as the perturbations decay over time. In contrast, the second solution exhibits the negative smallest eigenvalues, signifying instability due to the growth of perturbations. Consequently, based on the stability results, only the first solution is considered physically meaningful, even though the model generates two possible solutions. As the first solution proves to be the most reliable, we will focus on its implementation while preserving the second solution for potential future exploration.

4.3. P2SATRA

Since this study involves the ternary hybrid nanofluid, which is widely recognized for its superior heat transfer capabilities, we further analyze the heat transfer rate as measured by $\mathrm{Re}_x^{-1/2}Nu_x$. Additionally, as our stability analysis confirms that only the first solution is stable, we

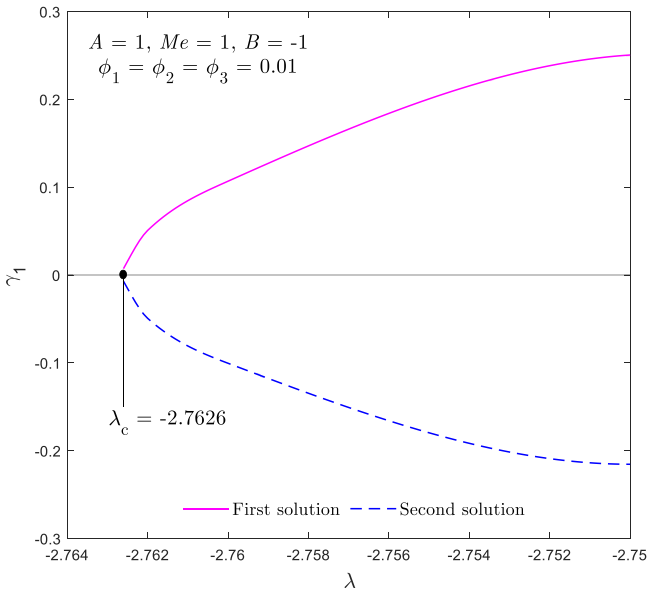

Fig. 10. Plot of the smallest eigenvalues (stability analysis).

focus on this first solution for further heat transfer rate analysis. To validate the findings, we employ logic mining using an artificial neural network model, referred to as P2SATRA [40]. All the variables and parameters derived from the experimentation conducted in the previous section are summarized in Table 5.

Table 6 presents the results of P2SATRA in classifying the numerical results of $\mathrm{Re}_x^{-1/2}Nu_x$. Two different k−cross validations were applied to avoid any bias towards the imbalanced class of $\mathrm{Re}_x^{-1/2}Nu_x$ results. With different logical rules retrieved by the model, the best final induced logic will be selected based on the values of Accuracy. The best final induced logic (highest Accuracy) selected to represent the overall relationship between the parameters to $\mathrm{Re}_x^{-1/2}Nu_x$, is formulated as follows,

$$\Gamma_{NUX} = (A \vee B) \wedge (\phi_2 \vee \lambda) \wedge (\phi_3 \vee Me). \tag{20}$$

This logic is visually represented by the corresponding logic gate circuit, as shown in Fig. 11, whereby the outcome of Γ_{NUX} can be deduced as the following:

i. $\Gamma_{NUX} = 1$: $(Me,\ A,\ B,\ \lambda,\ \phi_2,\ \phi_3) = (1,1,1,1,1,1)$.
ii. $\Gamma_{NUX} = -1$: $(Me,\ A,\ B,\ \lambda,\ \phi_2,\ \phi_3) = (-1,-1,-1,-1,-1,-1)$.
iii. $(A \vee B)$ dependent to each other due to the positioning of attributes via the permutation operator.
iv. $(\lambda \vee \phi_2)$ dependent to each other due to the positioning of attributes via the permutation operator.
v. $(\phi_3 \vee Me)$ dependent to each other due to the positioning of attributes via the permutation operator.

Table 5
Variables in P2SATRA.

Variable	Representing	Neuron representation via k-mean clustering
Ω_1	Me	1: Lower than 1.7182
ω_1	A	−1: Higher and equal to 1.7182
Ω_2	B	1: {−2, −3}
		−1: {−1}
ω_2	λ	1: {−1.1, −1.2}
		−1: {−1}
Ω_3	ϕ_2	1: Lower than 0.0136
ω_3	ϕ_3	−1: Higher and equal to 0.0136
Γ_{NUX}	$\mathrm{Re}_x^{-1/2}Nu_x$	1: Lower than −1.0874
		−1: Higher and equal to −1.0874

These five deductions regarding the parameters influencing heat transfer in hybrid nanofluid reveal significant interdependencies among them. Deduction (i) indicates that when all parameters—melting (Me), first-order velocity (A), second-order velocity (B), shrinking surface parameter (λ), and nanoparticle concentrations (ϕ_2 and ϕ_3)—are set to 1 (refer Table 5 for the neuron representation), the heat transfer rate is minimized. Conversely, deduction (ii) suggests that when −1 (refer to the real value range in Table 5) is set to these parameters, they may enhance heat transfer rates. In deduction (iii), the first-order velocity and second-order velocity are shown to depend on each other because according to the mathematical model, they are governed by the same boundary condition, which influences flow characteristics. Deduction (iv) highlights a strong correlation between the shrinking surface parameter and the volume fraction of copper nanoparticles, identifying this combination as the most effective parameter. Finally, deduction (v) establishes a correlation between the volume fraction of silver nanoparticles and the melting parameter, demonstrating their simultaneous impact on the heat transfer rate. Collectively, these deductions emphasize the intricate interplay of parameters that govern the heat transfer performance of the hybrid nanofluid.

5. Conclusion

This study investigates the stagnation point flow and heat transfer characteristics of a ternary hybrid nanofluid past a stretching/shrinking sheet, focusing on the influence of the melting parameter and second-order velocity slip. The model is solved numerically, yielding dual numerical solutions, but only one of these solutions is stable. The stable numerical solutions are validated using logic mining P2SATRA that uses an artificial neural network to understand the relationship between the heat transfer performance of the model with the considered parameters. The conclusions can be summarized as follows, specifically for the stable solution:

- As the melting parameter and second-order velocity slip increase, the skin friction coefficient and local Nusselt number increase, while the velocity and temperature profiles decrease.
- Minimizing the melting parameter and second-order velocity slip can potentially expand the range of solutions, thus delaying boundary layer separation.
- The most accurate final induced logic, selected to represent the overall relationship between melting effect, first and second-order velocity slip, shrinking parameter, volume fraction of copper and silver with the stable numerical solution of $\mathrm{Re}_x^{-1/2}Nu_x$, is $\Gamma_{NUX} = (A \vee B) \wedge (\phi_2 \vee \lambda) \wedge (\phi_3 \vee Me)$, achieved in the third fold of a 10-fold cross-validation, with an accuracy of 0.81818 and a precision of 0.87500.

It is important to note that these findings may be limited to the specific parameter ranges and thermal properties considered in this study. For future research, it is recommended to expand the investigation to include tetra and penta hybrid nanoparticles, as well as explore additional geometries, to enhance understanding of their impact on heat transfer performance and further increase the relevance of the findings. It is also encouraged that the present model be investigated experimentally to validate the theoretical results.

CRediT authorship contribution statement

Nur Ezlin Zamri: Writing – review & editing, Software, Methodology, Formal analysis, Data curation. **Nur Syahirah Wahid:** Writing – review & editing, Visualization, Software, Methodology, Investigation, Funding acquisition, Formal analysis, Data curation. **Nur Hazirah Adilla Norzawary:** Writing – review & editing. **Siti Zulaikha Mohd Jamaludin:** Validation, Methodology, Conceptualization. **Ioan Pop:**

Table 6
The formulation of final induced logic extracted from P2SATRA with accuracy, precision, sensitivity, specificity, and Matthew's correlation coefficient values.

k—fold		Final Induced Logic Extracted	Accuracy	Precision	Sensitivity	Specificity	Matthew's Correlation Coefficient
5	1	$(Me \vee \neg A) \wedge (\neg B \vee \lambda) \wedge (\neg \phi_2 \vee \phi_3)$	0.22727	0.00000	0.29412	0.00000	−0.59409
	2	$(A \vee B) \wedge (\lambda \vee \phi_2) \wedge (\phi_3 \vee Me)$	0.81818	0.82353	0.88000	0.73684	0.62750
	3	$(A \vee \phi_2) \wedge (Me \vee \neg B) \wedge (\lambda \vee \phi_3)$	0.68182	0.60000	0.60000	0.78947	0.38947
	4	$(\phi_3 \vee Me) \wedge (A \vee \neg \lambda) \wedge (B \vee \phi_2)$	0.61364	0.57692	0.52174	0.71429	0.23978
	5	$(\phi_3 \vee \phi_2) \wedge (Me \vee \lambda) \wedge (\neg A \vee B)$	0.56818	0.42857	0.57143	0.56250	0.12898
Average			0.58182	0.48580	0.57346	0.56062	0.15833
Maximum			0.81818	0.82353	0.88000	0.73684	0.62750
10	1	$(Me \vee \neg A) \wedge (B \vee \neg \lambda) \wedge (\neg \phi_2 \vee \phi_3)$	0.22727	0.00000	0.50000	0.00000	−0.59409
	2	$(B \vee A) \wedge (\phi_3 \vee Me) \wedge (\phi_2 \vee \lambda)$	0.70455	0.93333	0.94444	0.53846	0.50089
	3	$(A \vee B) \wedge (\phi_2 \vee \lambda) \wedge (\phi_3 \vee Me)$	0.81818	0.87500	0.91667	0.70000	0.63831
	4	$(A \vee B) \wedge (\phi_2 \vee \neg \lambda) \wedge (\phi_3 \vee Me)$	0.79545	0.66667	0.75000	0.87500	0.60193
	5	$(A \vee B) \wedge (\lambda \vee \phi_2) \wedge (Me \vee \phi_3)$	0.75000	0.66667	0.68000	0.84211	0.51938
	6	$(\phi_3 \vee A) \wedge (\phi_2 \vee \neg \lambda) \wedge (B \vee Me)$	0.63636	0.59259	0.52174	0.76190	0.29096
	7	$(A \vee B) \wedge (\phi_3 \vee \neg Me) \wedge (\lambda \vee \phi_2)$	0.61364	0.55556	0.50000	0.75000	0.25565
	8	$(\neg A \vee \neg B) \wedge (Me \vee \phi_3) \wedge (\lambda \vee \phi_2)$	0.59091	0.48000	0.51852	0.70588	0.22059
	9	$(\phi_2 \vee \neg \phi_3) \wedge (B \vee A) \wedge (Me \vee \lambda)$	0.59091	0.63636	0.60000	0.58333	0.18257
	10	$(\phi_2 \vee \neg \phi_3) \wedge (Me \vee B) \wedge (A \vee \lambda)$	0.56818	0.42857	0.57143	0.56250	0.12898
Average			0.62955	0.58347	0.65028	0.63192	0.27452
Maximum			0.81818	0.87500	0.91667	0.70000	0.63831

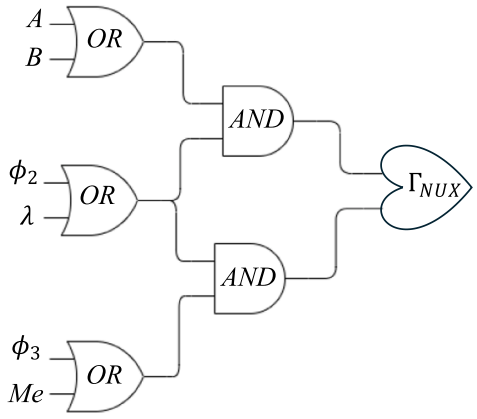

Fig. 11. Best final induced logic circuit illustration.

Writing – original draft, Supervision, Project administration. **Mohd Shareduwan Mohd Kasihmuddin:** Supervision. **Norihan Md Arifin:** Supervision. **Mohd. Asyraf Mansor:** Supervision.

Declaration of Competing Interest

The authors declare that they have no known competing financial interests or personal relationships that could have appeared to influence the work reported in this paper.

Acknowledgements

The authors acknowledged Universiti Putra Malaysia for the given Putra Grant [GP-IPM 9787700]. The support from Universiti Sains Malaysia, Babeş-Bolyai University, and Academy of Romanian Scientists are also being acknowledged.

References

[1] A. Alsaedi, S.A. Khan, T. Hayat, Mixed convective entropy optimized flow of rheological nanoliquid subject to Cattaneo-Christov fluxes: An application to solar energy, Energy 278 (2023) 127805, https://doi.org/10.1016/j.energy.2023.127805.

[2] Sami Ullah KhanWasim Jamshed, Finite Element Analysis and Wear Rate Analysis of Nano Coated High Speed Steel Tools for Industrial Application, Babylon. J. Mech. Eng. 2023 (2023) 13–19, https://doi.org/10.58496/BJME/2023/002.

[3] M. Sheikholeslami, Numerical investigation for concentrated photovoltaic solar system in existence of paraffin equipped with MWCNT nanoparticles, Sustain. Cities Soc. 99 (2023) 104901, https://doi.org/10.1016/j.scs.2023.104901.

[4] S.A. Sajadifar, A. Karimipour, D. Toghraie, Fluid flow and heat transfer of non-Newtonian nanofluid in a microtube considering slip velocity and temperature jump boundary conditions, Eur. J. Mech. - BFluids 61 (2017) 25–32, https://doi.org/10.1016/j.euromechflu.2016.09.014.

[5] H. Adun, D. Kavaz, M. Dagbasi, Review of ternary hybrid nanofluid: Synthesis, stability, thermophysical properties, heat transfer applications, and environmental effects, J. Clean. Prod. 328 (2021) 129525, https://doi.org/10.1016/j.jclepro.2021.129525.

[6] S. Manjunatha, V. Puneeth, B.J. Gireesha, AliJ. Chamkha, Theoretical Study of Convective Heat Transfer in Ternary ŕNanofluid Flowing past a Stretching Sheet, J. Appl. Comput. Mech. 8 (2022) 1279–1286, https://doi.org/10.22055/jacm.2021.37698.3067.

[7] S. Alshahrani, N.A. Ahammad, M. Bilal, M.E. Ghoneim, A. Ali, M.F. Yassen, E. Tag-Eldin, Numerical simulation of ternary nanofluid flow with multiple slip and thermal jump conditions, Front. Energy Res. 10 (2022) 967307, https://doi.org/10.3389/fenrg.2022.967307.

[8] S. Riaz, M.F. Afzaal, Z. Wang, A. Jan, U. Farooq, Numerical heat transfer of non-similar ternary hybrid nanofluid flow over linearly stretching surface, Numer. Heat. Transf. Part Appl. (2023) 1–15, https://doi.org/10.1080/10407782.2023.2251093.

[9] U.S. Mahabaleshwar, K.M. Nihaal, L.M. Pérez, H.F. Oztop, An analysis of heat and mass transfer of ternary nanofluid flow over a Riga plate: Newtonian heating, Numer. Heat. Transf. Part B Fundam. (2023) 1–16, https://doi.org/10.1080/10407790.2023.2282165.

[10] S.U. Jan, U. Khan, M.A. El-Rahman, S. Islam, A.M. Hassan, A. Ullah, Effect of variable thermal conductivity of ternary hybrid nanofluids over a stretching sheet with convective boundary conditions and magnetic field, Results Eng. 20 (2023) 101531, https://doi.org/10.1016/j.rineng.2023.101531.

[11] F.N. Jamrus, I. Waini, U. Khan, A. Ishak, Effects of magnetohydrodynamics and velocity slip on mixed convective flow of thermally stratified ternary hybrid nanofluid over a stretching/shrinking sheet, Case Stud. Therm. Eng. 55 (2024) 104161, https://doi.org/10.1016/j.csite.2024.104161.

[12] Z. Mahmood, U. Khan, S. Saleem, K. Rafique, S.M. Eldin, Numerical analysis of ternary hybrid nanofluid flow over a stagnation region of stretching/shrinking curved surface with suction and Lorentz force, J. Magn. Magn. Mater. 573 (2023) 170654, https://doi.org/10.1016/j.jmmm.2023.170654.

[13] Siti Shuhada Ishak, Mohd Rijal Ilias, Seripah Awang Kechil, Fazillah Bosli, Aligned magnetohydrodynamics and thermal radiation effects on ternary hybrid nanofluids over vertical plate with nanoparticles shape containing gyrotactic microorganisms, J. Adv. Res. Numer. Heat. Transf. 18 (2024) 68–91, https://doi.org/10.37934/arnht.18.1.6891.

[14] L. Roberts, On the melting of a semi-infinite body of ice placed in a hot stream of air, J. Fluid Mech. 4 (1958) 505–528, https://doi.org/10.1017/S002211205800063X.

[15] M. Epstein, D.H. Cho, Melting heat transfer in steady laminar flow over a flat plate, J. Heat. Transf. 98 (1976) 531–533, https://doi.org/10.1115/1.3450595.

[16] N. Bachok, A. Ishak, I. Pop, Melting heat transfer in boundary layer stagnation-point flow towards a stretching/shrinking sheet, Phys. Lett. A 374 (2010) 4075–4079, https://doi.org/10.1016/j.physleta.2010.08.032.

[17] S. Ahmad, I. Pop, Melting Effect on Mixed Convection Boundary Layer Flow About a Vertical Surface Embedded in a Porous Medium: Opposing Flows Case, Transp. Porous Media 102 (2014) 317–323, https://doi.org/10.1007/s11242-014-0291-x.

[18] T. Muhammad, H. Waqas, U. Farooq, M.S. Alqarni, Numerical simulation for melting heat transport in nanofluids due to quadratic stretching plate with

nonlinear thermal radiation, Case Stud. Therm. Eng. 27 (2021) 101300, https://doi.org/10.1016/j.csite.2021.101300.
[19] M.H. Shojaeefard, M. Jourabian, A.A. Rabienataj Darzi, A. Bayat, Inward melting inside a horizontal multilobed capsule with conductive wall affected by Ag-MgO/water hybrid and MgO/water nanofluids, J. Heat. Mass Transf. Res. 8 (2021), https://doi.org/10.22075/jhmtr.2021.22194.1326.
[20] N.S. Wahid, N.M. Arifin, I. Pop, N. Bachok, M.E.H. Hafidzuddin, MHD stagnation-point flow of nanofluid due to a shrinking sheet with melting, viscous dissipation and Joule heating effects, Alex. Eng. J. 61 (2022) 12661–12672, https://doi.org/10.1016/j.aej.2022.06.041.
[21] S. Sharma, A. Dadheech, A. Parmar, J. Arora, Q. Al-Mdallal, S. Saranya, MHD micro polar fluid flow over a stretching surface with melting and slip effect, Sci. Rep. 13 (2023) 10715, https://doi.org/10.1038/s41598-023-36988-3.
[22] A. Olkha, R. Choudhary, Investigation of Melting Heat Transfer in Viscous Nanofluid Flow Including Micro-Organisms and Entropy Generation Due to an Inclined Exponentially Stretching Sheet, J. Nanofluids 13 (2024) 446–463, https://doi.org/10.1166/jon.2024.2122.
[23] K. Sudarmozhi, D. Iranian, N. Alessa, Investigation of melting heat effect on fluid flow with brownian motion/thermophoresis effects in the occurrence of energy on a stretching sheet, Alex. Eng. J. 94 (2024) 366–376, https://doi.org/10.1016/j.aej.2024.03.065.
[24] N.H.A. Norzawary, N. Bachok, F.M. Ali, N.A.A. Rahmin, Double solutions and stability analysis of slip flow past a stretching/shrinking sheet in a carbon nanotube, Math. Model. Comput. 9 (2022) 816–824, https://doi.org/10.23939/mmc2022.04.816.
[25] N.H.A. Norzawary, N. Bachok, F.M. Ali, N.M. Arifin, Slip Flow Over an Exponentially Stretching/Shrinking Sheet in a Carbon Nanotubes with Heat Generation: Stability Analysis, J. Adv. Res. Fluid Mech. Therm. Sci. 108 (2023) 28–38, https://doi.org/10.37934/arfmts.108.1.2838.
[26] A.V. Roşca, I. Pop, Flow and heat transfer over a vertical permeable stretching/shrinking sheet with a second order slip, Int. J. Heat. Mass Transf. 60 (2013) 355–364, https://doi.org/10.1016/j.ijheatmasstransfer.2012.12.028.
[27] A.K. Abdul Hakeem, N. Vishnu Ganesh, B. Ganga, Magnetic field effect on second order slip flow of nanofluid over a stretching/shrinking sheet with thermal radiation effect, J. Magn. Magn. Mater. 381 (2015) 243–257, https://doi.org/10.1016/j.jmmm.2014.12.010.
[28] M.J. Uddin, W.A. Khan, A.I.Md Ismail, Melting and second order slip effect on convective flow of nanofluid past a radiating stretching/shrinking sheet, Propuls. Power Res. 7 (2018) 60–71, https://doi.org/10.1016/j.jppr.2018.01.003.
[29] S. Abu Bakar, N.S. Wahid, N.M. Arifin, N.S. Khashi'ie, The flow of hybrid nanofluid past a permeable shrinking sheet in a Darcy–Forchheimer porous medium with second-order velocity slip, Waves Random Complex Media (2022) 1–18, https://doi.org/10.1080/17455030.2021.2020375.
[30] D. Swapna, K. Govardhan, G. Narender, S. Misra, Viscous dissipation and Chemical reaction on Radiate MHD Casson nanofluid past a stretching surface with a slip effect, J. Heat. Mass Transf. Res. (2024), https://doi.org/10.22075/jhmtr.2024.31758.1477.
[31] W.L. Oberkampf, T.G. Trucano, Verification and validation in computational fluid dynamics, Prog. Aerosp. Sci. 38 (2002) 209–272, https://doi.org/10.1016/S0376-0421(02)00005-2.
[32] M. Alhadri, J. Raza, U. Yashkun, L.A. Lund, C. Maatki, S.U. Khan, L. Kolsi, Response surface methodology (RSM) and artificial neural network (ANN) simulations for thermal flow hybrid nanofluid flow with Darcy-Forchheimer effects, J. Indian Chem. Soc. 99 (2022) 100607, https://doi.org/10.1016/j.jics.2022.100607.
[33] S.R. Reddisekhar Reddy, S. Jakeer, V.E. Sathishkumar, H.T. Basha, J. Cho, Numerical study of TC4-NiCr/EG+Water hybrid nanofluid over a porous cylinder with Thompson and Troian slip boundary condition: Artificial neural network model, Case Stud. Therm. Eng. 53 (2024) 103794, https://doi.org/10.1016/j.csite.2023.103794.
[34] I. Waini, A. Ishak, I. Pop, Melting heat transfer of a hybrid nanofluid flow towards a stagnation point region with second-order slip, Proc. Inst. Mech. Eng. Part E J. Process Mech. Eng. 235 (2021) 405–415, https://doi.org/10.1177/0954408920961213.
[35] S. Jakeer, S.R.R. Reddy, A.M. Rashad, M. Lakshmi Rupa, C. Manjula, Nonlinear analysis of Darcy-Forchheimer flow in EMHD ternary hybrid nanofluid (Cu-CNT-Ti/water) with radiation effect, Forces Mech. 10 (2023) 100177, https://doi.org/10.1016/j.finmec.2023.100177.
[36] S.S. Ishak, M.R. Ilias, S.A. Kechil, Ternary Hybrid Nanofluids Containing Gyrotactic Microorganisms with Magnetohydrodynamics Effect over a Shrinking/Stretching of the Horizontal Plate, J. Adv. Res. Fluid Mech. Therm. Sci. 109 (2023) 102–230, https://doi.org/10.37934/arfmts.109.2.210230.
[37] J.H. Merkin, On dual solutions occurring in mixed convection in a porous medium, J. Eng. Math. 20 (1986) 171–179, https://doi.org/10.1007/BF00042775.
[38] P.D. Weidman, D.G. Kubitschek, A.M.J. Davis, The effect of transpiration on self-similar boundary layer flow over moving surfaces, Int. J. Eng. Sci. 44 (2006) 730–737, https://doi.org/10.1016/j.ijengsci.2006.04.005.
[39] S.D. Harris, D.B. Ingham, I. Pop, Mixed Convection Boundary-Layer Flow Near the Stagnation Point on a Vertical Surface in a Porous Medium: Brinkman Model with Slip, Transp. Porous Media 77 (2009) 267–285, https://doi.org/10.1007/s11242-008-9309-6.
[40] M.S.M. Kasihmuddin, S.Z.M. Jamaludin, MohdA. Mansor, H.A. Wahab, S.M. S. Ghadzi, Supervised Learning Perspective in Logic Mining, Mathematics 10 (2022) 915, https://doi.org/10.3390/math10060915.
[41] S.Z.M. Jamaludin, N.A. Romli, M.S.M. Kasihmuddin, A. Baharum, MohdA. Mansor, M.F. Marsani, Novel logic mining incorporating log linear approach, J. King Saud. Univ. - Comput. Inf. Sci. 34 (2022) 9011–9027, https://doi.org/10.1016/j.jksuci.2022.08.026.
[42] J. Kierzenka, L.F. Shampine, A BVP solver based on residual control and the Maltab PSE, ACM Trans. Math. Softw. 27 (2001) 299–316, https://doi.org/10.1145/502800.502801.
[43] L.F. Shampine, J. Kierzenka, M.W. Reichelt, Solving Boundary Value Problems for Ordinary Differential Equations in Matlab with bvp4c, (2004).